

7-12-2014

Observation and Measurement of the Growth of the Primary Instabilities of the Richtmyer-Meshkov Instability and Observation of Secondary Instabilities

Tennille Charisse Bernard

Follow this and additional works at: https://digitalrepository.unm.edu/me_etds

Recommended Citation

Bernard, Tennille Charisse. "Observation and Measurement of the Growth of the Primary Instabilities of the Richtmyer-Meshkov Instability and Observation of Secondary Instabilities." (2014). https://digitalrepository.unm.edu/me_etds/77

This Thesis is brought to you for free and open access by the Engineering ETDs at UNM Digital Repository. It has been accepted for inclusion in Mechanical Engineering ETDs by an authorized administrator of UNM Digital Repository. For more information, please contact disc@unm.edu.

Tennille Charisse Bernard

Candidate

Mechanical Engineering

Department

This thesis is approved, and it is acceptable in quality and form for publication:

Approved by the Thesis Committee:

Peter Vorobieff, Chair

C. Randall Truman

Dimiter Petsev

**OBSERVATION AND MEASUREMENT OF THE GROWTH
OF PRIMARY INSTABILITIES OF THE RICHTMYER-MESHKOV
INSTABILITY AND OBSERVATION OF SECONDARY INSTABILITES**

by

TENNILLE C. BERNARD

**B.S., MECHANICAL ENGINEERING
UNIVERSITY OF NEW MEXICO
2011**

**M.S., MECHANICAL ENGINEERING
UNIVERSITY OF NEW MEXICO
2014**

THESIS

Submitted in Partial Fulfillment of the
Requirements for the Degree of

Master of Science

Mechanical Engineering

The University of New Mexico
Albuquerque, New Mexico

04 April, 2014

Dedication

I dedicate this firstly to my father, Malcolm Bernard, who funded my undergraduate degree, but was not able to see me receive it. We always talked about me getting my Masters, and this is bringing me one step closer. Ich liebe dich. Ich vermisse dich. Vielen Dank für alles.

To my mother, Hillis Darylin Richards whose love convinced me that I could do anything, even when the world said I couldn't. You keep me going, Mommy, and I love you.

To my husband, Joshua Daniel Pacheco: We did it!

To everyone who helped me along the way: Mary Jastrzemski, Cindi Santistevan, Janine Pacheco, Deborah Chavez, Dr. Chris Hall, and anyone else I may have forgotten. I'm only here today thanks to your efforts, generosity, and willingness to work with me. Thank you.

Thank you all!

Acknowledgement Page

To everyone who helped me along the way: the Fluidities Team (Dell Olmstead, Jon Vigil, Clint Corbin, Garrett Kuehner, Patrick Wayne, Sanjay Kumar, Michael Anderson, Joe Conroy, and Ross White) and anyone else I may have forgotten. I'm only here today thanks to your efforts, generosity, and willingness to work with me. Thank you.

Finally, to my professors: Dr. Peter Vorobieff and Dr. C. Randall Truman. Thank you for giving me an opportunity. If it were not for you and the resources available to you, I certainly would not be one step closer to attaining my Master's degree.

This work was funded by the U.S. National Nuclear Security Agency (NNSA), DE-NA0002220.

Thank you all!

Observation and Measurement of the Growth of Primary Instabilities of the Richtmyer-Meshkov Instability, and Observation of Secondary Instabilities

by

Tennille C. Bernard

B.S., Mechanical Engineering, University of New Mexico, 2011

M.S., Mechanical Engineering, University of New Mexico, 2014

Abstract

The following thesis presents an experimental study observing and measuring the change in two of the key features of the Richtmyer-Meshkov (RM) instability in a shock-accelerated, initially cylindrical gas column; that is, the counter-rotating vortex pair and the central spike; and the observation of secondary instabilities within the primary instability. The formation of the instabilities is the result of a standing normal shock wave of air interacting with a cylindrical column of sulfur hexafluoride saturated with acetone. The experimental study is performed at two Mach numbers, 1.7 and 2.1, both with a maximum variation of 10% of either Mach number. The measurements of the size of these features of interest were compared to two external characteristics of the experiment: the actual timing after shock when the instability was measured and the distance downstream of the initial position of the cylindrical gas column. The development of the instability is tracked from the moment of shock impact until transition to turbulence when the flow becomes well-mixed. It was observed that the development of the instabilities with respect to the downstream distance point of observation was weakly correlated to the experimental Mach number. In contrast, a stronger correlation between the downstream distance and the feature size was evident. This behavior was previously observed for the

counter-rotating vortex pairs, but it is a new observation for the growth of the spike that forms due to shock focusing.

Contents

1 Introduction.....	1
1.1 History.....	3
1.2 Governing Equations.....	6
1.3 Goals of Study.....	9
2 History of Work Done on the Richtmyer-Meshkov Instability	11
3 Experimental Setup	17
3.1 Shock Tube.....	17
3.2 Injection System.....	21
3.3 Visualization.....	23
4 Post Processing Techniques	25
4.1 Measurement of the Counter-Rotating Vortex Pair and the Central Spike.....	25
4.2 Angle of the Camera/Mirror.....	26
5 Results	28
5.1 Mie Visualization	28
5.2 Numerics versus Mie Scattering	29
5.3 Experimental Results.....	31
6 Morphology Characteristics	37
6.1 RMI.....	37
6.2 Growth of the Counter-Rotating Vortex Pair and Central Spike	39

6.3 Shock Focusing	40
6.4 Secondary Instability Development	41
7 Conclusions.....	43
7.1 Future Work	44
References	45

List of Figures

1.1	Initial conditions injection system and a section of the test section.....	2
3.1.1	Drawing of the experimental apparatus.....	17
3.1.2	Photograph of the overall shock tube laboratory setup (tilted at a 30 degree angle to the horizontal). The control center (pictured in the middle) was where the data collection occurs.....	17
3.1.3	Solenoid driven puncture head in the driver section housing.....	19
3.1.4	Mylar distribution, flanges and latches.....	19
3.3.1	Right and Top view of Laser and lens system. The system is housed in a Lexan enclosure to protect the lenses from dust and accidental damage or shifting during experimental runs.....	23
4.1.1	Measurement of the streamwise extent and spike length of an RMI image.....	25
4.2.1	Layout of mirror to the top of the test section.....	26
5.3.1	Plot of Counter-Rotating Vortex Pair Length vs. Actual Timing for Mach 1.7 and Mach 2.1 experimental runs.....	32
5.3.2	Plot of Spike Length vs. Actual Timing for Mach 1.7 and Mach 2.1 experimental runs.....	32
5.3.3	Plot of Counter-Rotating Vortex Pair Length vs. Downstream Distance for Mach 1.7 and Mach 2.1 experimental runs.....	33

5.3.4	Plot of Spike Length vs. Downstream Distance for Mach 1.7 and Mach 2.1 experimental runs.....	33
5.3.5	Experimental flow visualization using PLIF and Mie scattering of droplets for three Mach numbers. Flow direction is from left to right. Experimental images are inverted, so darker areas correspond to flow seeded with droplets (label “Mie”) or marked with acetone tracer (labeled “PLIF”). Extent of imaged area is 10.09 cm. Individual image timings (with time = 0 corresponding to shock reaching the center of the gas column) are labeled.....	34
6.1.1	Inverted color image capture of an RMI with key features indicated. Note the counter-rotating vortex pair, the spike, and the lion’s tail, or small scale counter- rotating vortex pair located at the end of the spike.....	36
6.3.1	Numerical simulation of transition from initial conditions to spike development due to shock focusing. The image on the left shows the circular pre-shock initial conditions. The image on the right includes an overlay of the initial conditions on the post-shock RMI. The initial conditions, acting as a lens, focuses the high pressure region to a point of convergence.....	38
6.4.1	A numerical simulation of RMI. The colored area of the counter-rotating vortex pair consists of secondary instabilities, such as KHI and baroclinic instabilities.....	39

Chapter 1

Introduction

Where two fluids of different densities meet, there will be an interface. Disturbing this interface will generate instabilities, and the type of instability is determined by how the interface was disturbed. A fluid interface under the influence of gravity (in the case of a denser fluid vertically above a lighter fluid) will result in a Rayleigh-Taylor Instability (RTI) [1]. The energy that powers this instability is as a direct result of the action of gravity. Once the denser fluid has replaced all the lighter fluid at the bottom of the vessel, the system receives no more energy. In comparison, when the interface between two fluids of different densities is impulsively accelerated (either vertically or horizontally) the resulting disturbance is called the Richtmyer-Meshkov Instability (RMI) [2]. The development of this instability is due to a misalignment of the density and pressure gradients, resulting in the deposition of vorticity on the interface, and any initial perturbation of the interface then grows with time until it transitions to pure turbulent

flow. Unlike the RTI, the energy driving RMI is supplied in a very short time interval by the impulsive acceleration and then the system evolves to a stable state with no further outside energy input.

Past experimental data have shown that quasi two-dimensional RMI evolution from an initially cylindrical density interface is dominated by a counter-rotating vortex pair (CRVP), with secondary instabilities eventually leading to turbulence. This was seen only in the case of an experimental setup involving a planar gas cylinder, like in the experimental setup used for this thesis (Figure 1.1).

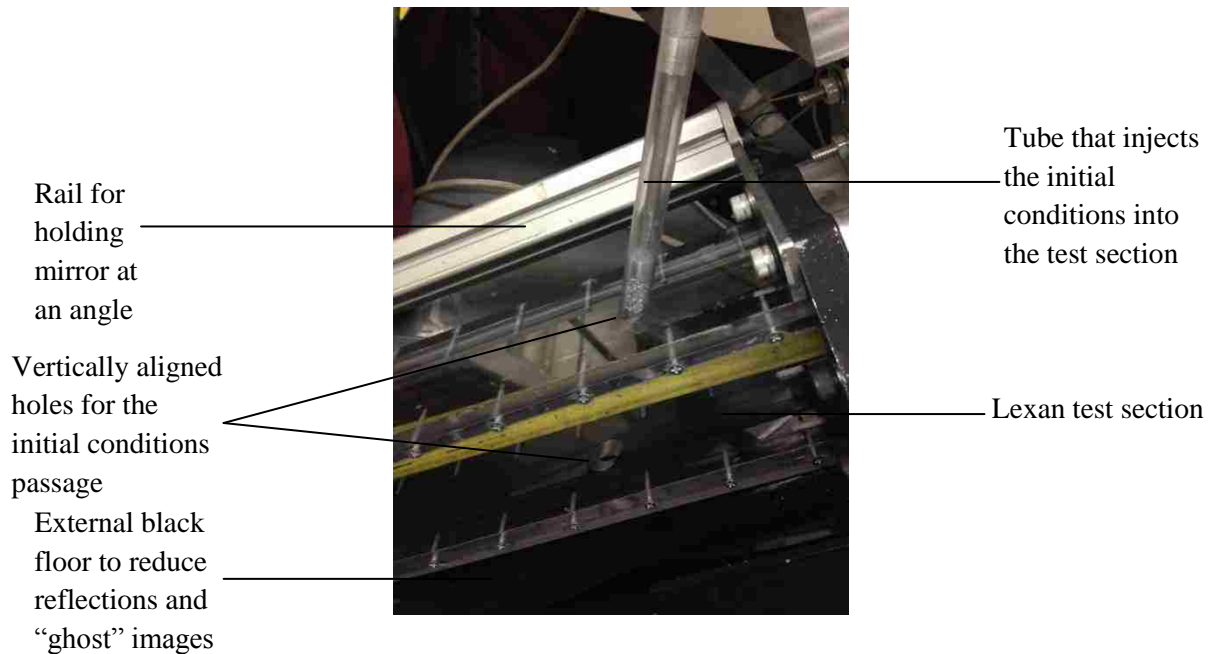


Figure 1.2: Initial conditions injection system and a section of the test section.

Here, a column of initial conditions gaseous fluid medium is forced to take the shape of a cylinder (usually by passing it through a cylindrical tube under the force of gravity) and injected into the test section. There is a hole under the test section which allows the heavy gas column to

exit and helps keep the laminar flow and cylindrical shape of the column, preventing the fluid from filling the test section and the rest of the shock tube with initial conditions. The resulting instability is visualized along the center plane of the column.

However, numerical studies performed by Anderson et al. [3] suggest that this is an incomplete description of the RMI. Anderson suggests that the RMI for a shocked gas cylinder also includes a central spike formed from the trailing line of the gas cylinder, and this spike is terminated by another small pair of counter-rotating vortices. It was determined that the use of Mie visualization, in the form of glycol droplets illuminated by a visible-light laser was not as effective in tracing the development of the RMI as the experimental method presented here: the use of acetone gas saturating the gaseous column of initial conditions and illuminated by an ultraviolet (UV) laser. When using the latter visualization method, the experimental data match the numerical data much better than when Mie scattering was used.

This thesis will examine the correlation between the Mach number of the shock wave and the growth of the RMI by measuring the two largest features of the flow. This will be measured against the actual timing of the shock wave and the distance downstream from the injection point of the column of initial conditions (the second fluid), to determine if time or distance is of greater consequence to the development of RMI. There will be discussion on the development of RMI, and proposed reasons for the flow morphology observed.

1.1 History

If one is to consider the history of RMI, then one should start by acknowledging the most common instabilities at the interface of two fluids. The most common instability is the Kelvin-

Helmholtz Instability (KHI). In 1868, Hermann von Helmholtz theorized that a significant velocity difference across the interface between two fluids (that may or may not be of the same density) that resulted in the evolution of vortices across the interface. When the growth of these vortices becomes large enough they can have enough energy, resulting in instability that deteriorates into turbulence. William Thomson, the 1st Baron Kelvin, followed up on this theory in 1871 [3]. KHI can be seen in everyday life in clouds and ocean waves.

The Rayleigh-Taylor Instability (RTI) can be considered the “parent” of RMI. A theory put forward in 1883 by John William Strutt, the 3rd Baron Rayleigh describes RTI as an instability at the interface of two immiscible fluids of different densities when one of the fluids is under constant acceleration into the other. Sir Geoffrey Ingram Taylor, OM, realized that this theory could be applied to other types of acceleration besides gravity [3]. Rayleigh considered an experiment where a denser fluid was suspended over a lighter one, both of which are acting under the Earth’s gravitational acceleration. At first, the interface between the two liquids can be modeled as planar, but under the constant acceleration, the denser fluid begins to move downward. The lighter fluid, in response, begins movement upwards in a “finger-like” pattern” [4], developed due to the growth of initial disturbance at the interface. Taylor noticed that the same situation would occur when, under an artificial acceleration, the lighter liquid was forced into the heavier liquid.

Using the theory behind RTI, in 1960 Robert D. Richtmyer predicted the Richtmyer-Meshkov instability: an instability at the interface of two immiscible fluids of different densities when one of the fluids is under an impulsive acceleration into the other. The result is said to be the impulsively-accelerated limit of RTI. Richtmyer’s theory was experimentally verified by E. E. Meshkov nine years later. Richtmyer considered a system consisting of two inviscid,

incompressible fluids with a sharp, well defined interface between them. This interface was made to undergo an acceleration profile in the form of a delta function. From this, a hydrodynamic instability develops because of the misalignment of the pressure and density gradients. The misalignment generates vorticity.

The two factors that determine the amount of vorticity deposited are the strength of the pressure gradient and the strength of the density gradient. The former is measured by the strength of the impulsive acceleration, specifically, the Mach number, M ($M = v/c$, where v is the velocity of the shock front and c is the speed of sound in the medium). As for the strength of the density gradient, the Atwood number, as defined below is used.

$$A = \frac{\rho_2 - \rho_1}{\rho_2 + \rho_1} \quad (1.2)$$

ρ_1 and ρ_2 represent the densities of air and second gas respectively.

According to the Richtmyer's linear stability theory, the development of RMI begins with a small perturbation of the amplitude that follows an initial linear growth with time. This linear period is followed by a non-linear period defined by "bubble and spike" instability: spikes when a heavier fluid penetrates a lighter fluid and bubbles when a lighter fluid penetrates a heavier one. This non-linear period evolves into full turbulence, as KHI and possibly other instabilities also develop at the interface and the two fluids mix.

One of the key differences between RTI and RMI is how the perturbations develop. RTI can only occur when the heavy fluid is "above" the lighter fluid with respect to the direction of the acceleration (for example, due to gravity). The perturbations of RTI grow exponentially with time for a sufficiently small amplitude. With RMI, the fluid is under an impulsive acceleration,

so relative position to the other fluid is of no importance. As a result, the RMI grows at a nearly constant rate at early timings.

1.2 Governing Equations

In any velocity field, the vorticity (or curl) is defined as

$$\vec{\omega} = \vec{\nabla} \times \vec{v} \quad (1.2.1)$$

The vorticity is like a vector whose magnitude is related to the rotational motion of an element of a fluid and whose direction is perpendicular to this motion. The vorticity production equation was derived from the Navier-Stokes equation (equation 1.2.2). The material derivative $\frac{DQ}{Dt}$ is defined in equation 1.2.3. \vec{v}, \vec{g}, P, μ represent the velocity, body forces (gravity), pressure and dynamic viscosity respectively. The resulting vorticity equation for an inviscid fluid and no body forces is shown by equation 1.2.4

$$\rho \frac{D\vec{v}}{Dt} = \rho \vec{g} - \vec{\nabla} P + \mu \vec{\nabla}^2 \vec{v} \quad (1.2.2)$$

$$\frac{D}{Dt} = \frac{d}{dt} + \vec{v} \cdot \vec{\nabla} \quad (1.2.3)$$

$$\frac{D\vec{\omega}}{Dt} = (\vec{\omega} \cdot \vec{\nabla}) \vec{v} - \vec{\omega} (\vec{\nabla} \cdot \vec{v}) + \frac{\vec{\nabla} \rho \times \vec{\nabla} P}{\rho^2} \quad (1.2.4)$$

In the last equation the first term represents the vorticity generation as a result of the velocity gradient (vortex stretching). The second term is the vorticity generation due to the compressibility. With the initial vorticity of the flow equal to zero, this reduces both terms to

zero. The third term represents the baroclinic vorticity production, which represents the generation of vorticity due to the misalignment of the pressure and density gradients.

Richtmyer proposed a growth equation to describe how the perturbations grew with time (equation 1.2.5).

$$\frac{d\eta}{dt} = k\Delta UA\eta_0 \quad (1.2.5)$$

η is growth of the amplitude of small perturbations, t is the time, k is the wavenumber, given by $k = \frac{2\pi}{\lambda}$ (or twice pi divided by the perturbation wavelength), A is the Atwood number, ΔU is the piston velocity and η_0 is the initial perturbation amplitude.

In general, there are certain equations that can be used to describe the behavior of a shock wave before, during, and after shock passage. These equations are used to describe a standing normal shock wave passing through perfect gas [5]. In a standing normal shock wave, a stationary wave front is perpendicular to the direction of flow.

$$\frac{p_1 M_1}{\sqrt{T_1}} = \frac{p_2 M_2}{\sqrt{T_2}} \quad (1.2.6)$$

$$T_1 \left(1 + \frac{\gamma-1}{2} M_1^2\right) = T_2 \left(1 + \frac{\gamma-1}{2} M_2^2\right) \quad (1.2.7)$$

$$p_1 (1 + \gamma M_1^2) = p_2 (1 + \gamma M_2^2) \quad (1.2.8)$$

The symbols are as follows: γ is the specific heat ratio; and the state variables p_1, p_2, M_1, M_2, T_1 and T_2 are the pressures, Mach numbers, and temperatures before and after the shock wave has occurred. If we define the state before the shock with $p_1, M_1,$ and $T_1,$ we have enough

information to calculate the state after the shock occurs. For example, to calculate the pressure ratio $\frac{p_2}{p_1}$ once can manipulate equation 1.2.8 to give

$$\frac{p_2}{p_1} = \frac{1 + \gamma M_1^2}{1 + \gamma M_2^2} \quad (1.2.9)$$

A value for M_2 can be calculated as shown below

$$M_2^2 = \frac{M_1^2 + \frac{2}{\gamma-1}}{\frac{2\gamma}{\gamma-2} M_1^2 - 1} \quad (1.2.10)$$

One should note that the value of M_2 is dependent only on M_1 and γ . Combining equations 1.2.8 and 1.2.9 reduces the number of variables required to calculate the pressure ratio from three to two.

$$\frac{p_2}{p_1} = \frac{2\gamma}{\gamma+1} M_1^2 - \frac{\gamma-1}{\gamma+1} \quad (1.2.11)$$

Utilizing a similar procedure, we can generate an expression for the temperature ratio

$$\frac{T_2}{T_1} = \frac{(1 + [\frac{\gamma-1}{2}] M_1^2) ([\frac{2\gamma}{\gamma-1}] M_1^2 - 1)}{\frac{\gamma+1}{2(\gamma-1)} M_1^2} \quad (1.2.12)$$

Combining equations 1.2.11 and 1.2.12 we can show the pressure ratio in terms of M_1 and γ .

$$\frac{p_2}{p_1} = \frac{(\gamma+1) M_1^2}{(\gamma-1) M_1^2 + 2} \quad (1.2.13)$$

This ratio is as of a direct result of the gas compression [5].

As mentioned above, the preceding equations are for a standing normal shock wave and assumed to be applicable for only perfect gases. In the experiment presented here, the use of sulfur hexafluoride gas saturated with acetone does not deviate from this ideal by much. For an ideal

gas, the intermolecular forces are assumed to be zero, the volume of the particles is negligible compared to the volume of the container it occupies and only elastic collisions occur between the particles and the walls of the container. This simplifying assumption reduces the equations to a simpler form; if not, one would have to include correction factors and the effects of the intermolecular forces in the equation and final results. In these experiments, sulfur hexafluoride experiences real gas effects, including the intermolecular forces when under compression (like during the initial stages of shock).

The choice to use sulfur hexafluoride was based on the ability to get the highest possible Atwood number from a gaseous medium that was also safe to use. Sulfur hexafluoride has a high density, which would then result in a higher overall Atwood number, defined below, where ρ_1 and ρ_2 represent the densities of air and second gaseous fluid medium respectively.

$$A = \frac{\rho_2 - \rho_1}{\rho_2 + \rho_1} \tag{1.2.14}$$

1.3 Goals of Study

The experiment presented here is in support of recent numerical work done regarding oblique shock wave interactions with gas column cylinders. This work seeks to experimentally validate the data provided by the numerical work. The need for an experimental validation of numerically simulated work is of great significance due to the fact that it is critical to understanding the processes by which fluid instabilities develop with respect to time and distance from the incidence of shock. There are some numerical observations which have not been

experimentally validated. The work presented here seeks to confirm the observations of Anderson et al. with respect to two key characteristics in RMI development, and provide conclusions about how these characteristics came to be.

Some additional discussions will be presented to elucidate on the causes behind the occurrence of some features that were first observed in the numerical simulations of Anderson et al. The measurement of these features was not considered as part of this thesis.

Chapter 2

History of Work Done on the Richtmyer-Meshkov Instability

The first mention of RMI was done in a paper authored by Richtmyer in 1960. [6] In this, he discussed work previously done by G.I. Taylor on the Rayleigh-Taylor instability. Richtmyer's paper went further to consider the case of impulsive acceleration where compressibility cannot be neglected. Richtmyer considered a linear model for a shock moving from a light fluid to a heavy fluid, based on Euler's work. Meshkov was able to prove that this proposed instability existed in 1969 by use of a shock tube. Like Richtmyer, Meshkov's experiments considered a shock moving from a light to a heavy fluid, but he also considered the reverse case of a heavy fluid impulsively penetrating a light fluid.

Within the same decade, Rudinger and Somers presented theoretical and experimental studies on the behavior of spherical and cylindrical gas bubbles impulsively accelerated by shock waves,

with the intent to use the bubbles as passive tracers in the flow. The bubbles were created from hydrogen, helium, and sulfur hexafluoride and measured using a schlieren system. Their results determined that bubble displacement, for gases lighter than air, was larger than the surrounding air, and the converse was true for gases heavier than air. Rudinger and Somers also proposed an expression that related the bubble velocity to the gas velocity by considering the formation of a vortex shape (a ring for a spherical bubble and a vortex pair for a cylindrical bubble). This expression is shown in equation 2.1.

$$\frac{u_b}{u_g} = 1 + \frac{2(1-\sigma)}{\pi^2(1+\sigma)} \quad (2.1)$$

u_b is the bubble velocity, u_g is the gas velocity, and σ is the ratio of bubble to gas densities ($\sigma = \frac{\rho_b}{\rho_g}$). Equation 2.1 can be rewritten using an Atwood number (Equation 2.2)

$$\frac{u_b}{u_g} = 1 - \frac{2A}{\pi^2} \quad (2.2)$$

In 1987, Haas and Sturtevant conducted experiments to observe planar shock waves that interact with cylindrical or spherical volumes of gas. They used helium and R22 to test cases of cylindrical and spherical initial conditions, respectively, and shock waves of Mach 1.2. The initial conditions were 5 cm in diameter and were generated by filling a shape created by stretching a 0.5 micrometer nitrocellulose membrane around two Pyrex disks of thickness 3 millimeters (that the ends of the cylinder). Haas and Sturtevant used a spark shadowgraph optical system to visualize the deformation of the initial conditions after the shock wave occurred. They compared their results for the velocities of the instabilities to the linear stability analysis from Richtmyer and Rudinger's theory, finding that the experimental velocities in the results were larger than the predicted values. This was primary due to the wall effects of the shock tube.

Picone and Boris in 1988 used the experimental results that Haas and Sturtevant generated to validate numerical simulations using the fluid dynamics code FAST2D. FAST2D considers inviscid, compressible fluid dynamics to solve Euler equations using a flux corrected transport method. Picone and Boris found a solid qualitative agreement between both their numerical simulation data and the experimental data of Haas and Sturtevant, and the recorded velocities of the upstream and the downstream edges of the instability. Picone and Boris' numerical data were also used to examine the vorticity generated by the shock wave interaction with the bubble, and to verify Picone's proposed non-linear theory for the late timing vorticity.

In 1993, J. W. Jacobs conducted experiments using sulfur hexafluoride cylindrical columns and helium at low Mach numbers ($M = 1.095$). Jacobs pioneered studies of shock wave interactions using initial conditions consisting of a laminar jet of gas, which eliminated the need for a membrane that would have separated the initial conditions from the surrounding atmosphere. As the membrane was not a passive instrument (affecting initial condition flow structure and disrupting visualization) this proved to be an advantage. Jacobs' experimental cylindrical column was 0.8 centimeters in diameter, considerably smaller than the diameter of the initial conditions in experiments performed by Haas and Sturtevant. The initial conditions were seeded with bi-acetyl gas, which had the ability of fluorescing with a 430 nm wavelength laser source that was manipulated into a planar sheet. Called Planar Laser Induced Fluorescence (PLIF), this method was used to visualize cross-sectional areas of the resulting fluid instabilities. The PLIF images were very much like the experimental image results of Haas and Sturtevant in morphology. Jacobs observed the formation of KHI for late times for sulfur hexafluoride initial conditions at the edge of the counter rotating vortex pair. Jacobs was able to compute the displacement of the instability as a function of time; he found that the theory of Rudinger and

Somers provided a final velocity of the counter-rotating vortex pair that was lower than the experimentally determined velocity.

Rightley, Vorobieff, and Benjamin performed a series of shock tube experiments in 1997 involving a gas curtain of sulfur hexafluoride impulsively accelerated by a Mach 1.2 shock wave. Visualization was done using the glycol droplet seeding method. Rightley et. al. executed experiments which took quantitative measurements of the width of the instability as it mixed and used a point vortex row model based off the work of Jacobs et. al. to calculate the circulation Γ . Rightley et. al. performed analysis of the ability of the glycol droplets to follow the flow in acting as a passive tracer. Their calculations showed a 3 microsecond delay for a particle of 0.5 micrometers of diameter to catch up with the piston velocity behind the shock. The conclusion was the particles do not follow the flow perfectly, but closely enough that the droplet particles can follow the formed instability and produce reasonably accurate data from the post-shock flow. In 1998, Rightley and his team continued this experimental setup to investigate the transition of RMI to turbulence. They used second-order structure functions based on the concentration of light scattered by the gas curtain. The team performed experimental runs for initial conditions with regular and multi-mode perturbations. From this, they discovered that the structure function approaches power-law behavior with an exponent close to $2/3$ as the gas curtain approached a fully mixed state; often seen as a signature characteristic of fully developed turbulence.

Vorobieff continued a similar series of experiments using Particle Image Velocimetry (PIV) measurements with a new team of Prestridge, Rightley and Benjamin. The benefit of the PIV was that it permitted the creation of velocity fields that were used to calculate the circulation in the flow. The circulation found was in good agreement to the model of circulation offered by Rightley.

In 2002, Zoldi compared experimental and numerical treatments of a cylindrical column of sulfur hexafluoride also accelerated by a shock of Mach number 1.2. The initial conditions were also seeded with glycol droplets and visualization was done using PIV. The numerical validation was done using the code RAGE: a multi-dimensional, adaptive mesh Eulerian hydrodynamic code. Zoldi performed the experiments at the same facility as Rightley, Vorobieff, and Prestridge. Zoldi's numerical results were in good qualitative agreement with experimental ones. When quantitative analysis was performed between Zoldi's experimental and numerical results (done by comparing the instability's height and width, the counter-rotating vortex pair spacing, the convective velocity and the circulation) the images showed that sulfur hexafluoride cylinder was bigger and more dispersed than the pattern of the glycol droplets that was used as a passive tracer. It should be noted that, in order to match the experimental results, the concentration of the sulfur hexafluoride was decreased to 60% and the density gradient was scattered to remove a distinct interface between the initial conditions and the air.

In 2010, Ukai conducted numerical simulations for traditional and multi-phase RMI where there was a single-mode perturbation. These simulations considered 3 cases: a light to heavy case with no particle tracers, a light to heavy case with particle tracers, and a light gas accelerated into a region with tracers and no heavy gas. Ukai found that the Stokes number (St , a measure of particle response time over some characteristic distance) and seeding density are key factors in how the particles responds to the shock wave. The particles behaved as passive tracers, with nearly instantaneous acceleration for low Stokes numbers ($St \ll 1$), and the instability follows RMI and Richtmyer's theory. For a large Stokes number, the particles moved relative to the flow, and acceleration was non-impulsive. This would give a Rayleigh-Taylor instability behavior.

From 2007, Vorobieff and Truman led a team of students at the University of New Mexico in performing experimental validation of RMI under multi-phase conditions using cylindrical column initial condition using both glycol fog droplets and PLIF with acetone. Experiments were performed at Mach 1.13, 1.2, 1.7, and 2.01, and at angles 0, 15 and 30 degrees to the horizontal.

Chapter 3

Experimental Setup

All experiments performed for this thesis were done at the Shock Tube facility at the University of New Mexico, Mechanical Engineering Department. For each experimental run, at least two images were taken: a background shot and a dynamic shot; with the intent that the background shot would be subtracted from the dynamic shot to make the final processed image as clear as possible. Both images were taken in grayscale.

3.1 Shock Tube

The tiltable 6061-T6 aluminum shock tube consisted of four sections: (1) a driver section with a thin film Mylar diaphragm that separated the driver section from (2) a driven section, connected to (3) a Lexan test section which emptied into (4) a runoff section. Figure 3.1.1 shows a drawing of the experimental apparatus while Figure 3.1.2. shows the actual setup of the facility. Each

section connected to the other using 6061-T6 aluminum flanges drilled with octagonal bolt pattern.

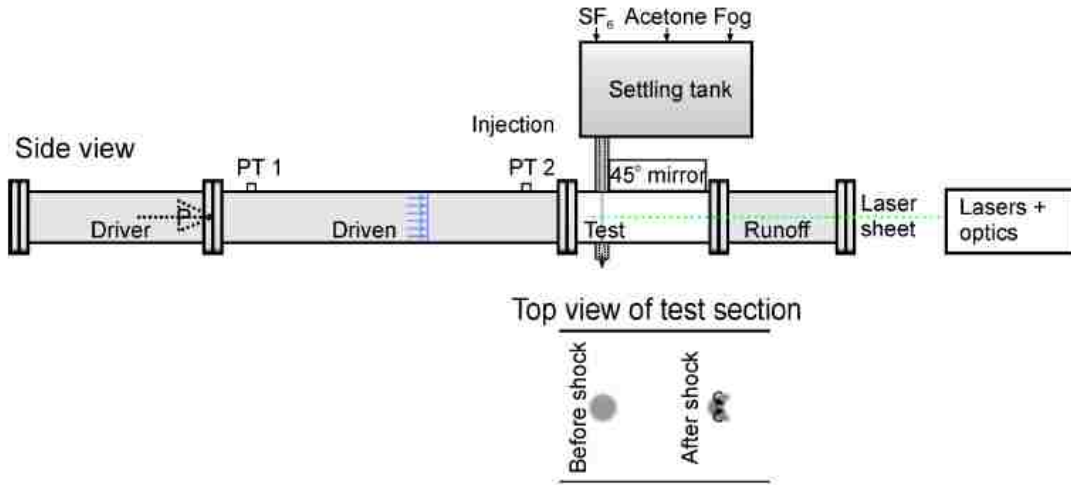


Figure 3.1.1: Drawing of the experimental apparatus.



Figure 3.1.2.: Photograph of the overall shock tube laboratory setup (tilted at a 30 degree angle to the horizontal). The control center (pictured in the middle) is where the data collection occurs.

The driver section had a circular, cross-sectional area of 3.75 inches outer diameter and 2.75 inch inner diameter. The circular cross-section was to eliminate high stress concentrations which would build up in a non-circular cross-section during the repetitions of the experimental procedure. This section also housed a shaft connected to an electronic-driven solenoid which, upon use of an external trigger, actuated an arrow-head shaped puncturing bit through the Mylar separating the driver section from the driven section (Figure 3.1.3, 3.1.4) The driven section was of a four square inches outer size (three square inch inner size) cross-sectional area, and made of the same type of Aluminum as the driver. Along the top of the driven section were two pressure transducers, located 2.59 meters apart. A pair of aluminum flanges connected the driven section to the test section, which was also a four square inch cross-sectional area. Using Lexan in the test section, instead of aluminum, allowed for undistorted views of the instabilities as they develop in each experimental run. The test section also included a pair of holes at the upstream side of the section. These holes, located at the top and bottom faces of the test section, were placed so that the initial conditions may fall vertically through both holes under the influence of gravity.

(Figure 1.1)

The injection system, from which these initial conditions originated, will be discussed in the next section. The runoff section, which ensured that the shock holds its shape well after it passes the test section, was connected to the downstream edge of the shock tube. The shock tube was kept immobile during the experiment by a system of C and I beams attached to a concrete wall at the downstream end of the shock tube.

The mechanism by which the experiments were performed as follows: The driver section was pressurized using helium gas until a specified pressure reading (85 ± 5 psi for Mach 1.7 and 180 ± 5 for Mach 2.1, with a no more than 10% variation in either Mach number).



Figure 3.1.3: Solenoid driven puncture head in the driver section housing.

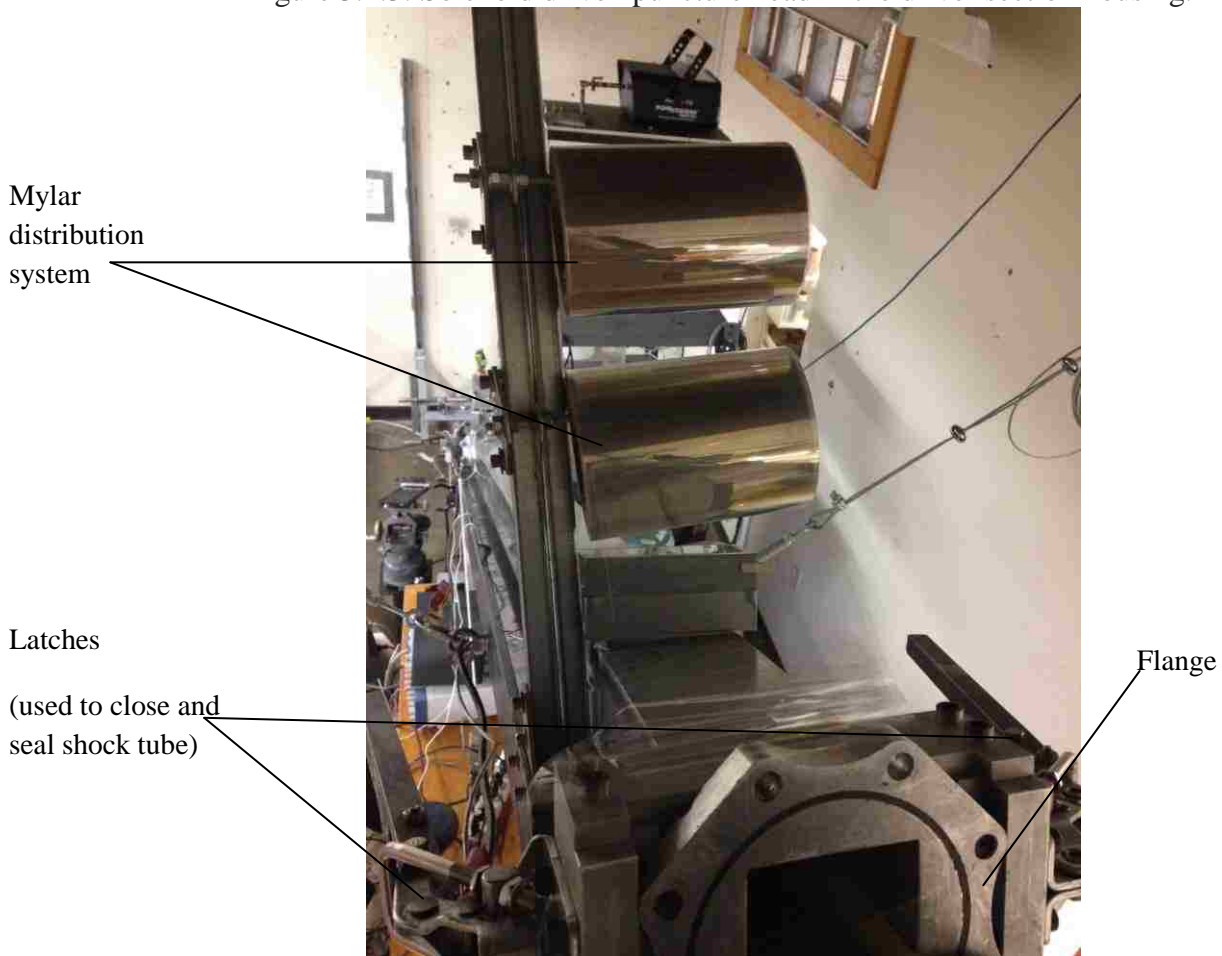


Figure 3.1.4: Mylar distribution, flanges and latches.

At this time, the external trigger was pressed so that the Mylar was punctured and a shockwave was generated. The shock wave traveled past two pressure transducers that recorded the shock speed and validated the quality of the shock wave. The shock wave then interacted with the initial condition column in the test section, generating the Richtmyer-Meshkov instability, and eventually the flow volume of interest was advected out of the test section. The evolution of the instability at different locations downstream and different time intervals was recorded by imaging the test section.

The images taken were measured to determine the growth of the central spike of the RMI (spike growth) with respect to time and downstream distance and the streamwise extent growth of the RMI (vortex growth) with respect to time and downstream distance. Vortex pair size and spike length were measured as shown in Figure 4.1.1, and is section Post-Processing Techniques.

3.2 Injection System

For the experiment, the initial conditions were cylindrical, comprised of sulfur hexafluoride (SF₆) with about 1% by volume of acetone tracer. SF₆ was bubbled through liquid acetone and the resulting vapor fluoresces strongly in ultra-violet light. The gas mix was stored in a reservoir tank (of dimensions 12'' x 20 '' x 16''). This reservoir also held a container of ice to reduce the temperature of the vapor, which helped stabilize the vapor as it exited the injection system, giving a laminar flow through the test section and out the exit hole for at least 6 inches. The vapor flowed from the reservoir to the test section via gravity through an injection nozzle that is 6.35mm in diameter.

The density of the vapor was calculated directly using a precision scale and a lightweight plastic container of known volume. The container was placed in the reservoir and allowed to fill with the vapor of the experiment. The container was covered with a lid, removed from the reservoir, and placed on the scale. The mass was recorded, and the container was opened, emptied and weighed again. The difference in mass between the full container and the empty container (with the lid) was used in the calculation of ρ_2 . This process was repeated multiple times to produce a good average density value. This value, in combination with the density of air (ρ_1) was then used below to calculate the Atwood number. Based on the values for ρ_1 and ρ_2 , the Atwood number was 0.5.

3.3 Visualization

Laser pulses were used to illuminate a horizontal plane in the test section, at a height of 3.81 cm from the floor of the section. The lasers were New Wave Gemini, whose original frequency (1066 nm) can be doubled or quadrupled to produce 532 nm or 266 nm pulses respectively, with a pulse duration of about 5 ns. The latter produced fluorescence with acetone with a fluorescence wavelength of about 480 nm. The laser beam was projected through a combination of spherical and cylindrical lenses mounted on an optical rail (connected to the laser beam head assembly for stability) to create a laser sheet (Figure 3.3.1). With the assistance of a mirror oriented appropriately, the laser sheet illuminated a horizontal plane.

Shock arrival at the first transducer triggered the NI-Scope software used to record the pressure traces from both transducers. Shock arrival at the second transducer was used to trigger the lasers via a delay generator. The delay generator acted as a timer for the laser pulses that acted as the “flash” for each exposure. The delay allowed for each shot to be double exposed.

The images were captured using an Apogee Alta U42 camera (pixel resolution 2048 x2048 at 16 grayscale bits per pixel). This camera contained a CCD that is both backward-facing and thermoelectrically-cooled, and the resulting quantum efficiency is about 90% for a range of wavelengths from 480 to 670 nm.



Figure3.3.1: Right and top views of Laser and lens system. The system is housed in a Lexan enclosure to protect the lenses from dust, accidental damage and shock wave effects during experimental runs.

Chapter 4

Post Processing Techniques

To obtain the data from each shot, certain measurements, corrections and equipment positions were employed. The following subsections of Chapter 4 will discuss these in depth.

4.1 Measurement of the Counter-Rotating Vortex Pair and the Central Spike

Two morphological features of the flow were measured: the streamwise extent or width of the counter-rotating vortex pair and the length of the central spike that forms due to shock focusing as the shock wave traverses the initial conditions. Figure 4.1.1 shows the measurements against an RMI image.

The choice of these measurements was made partially to compare with past work done on RMI evolution of cylindrical gas columns. Earlier studies also reported the streamwise extent of the vortex pair. The spike, however, was not quantified by these studies, likely because it was not properly resolved.

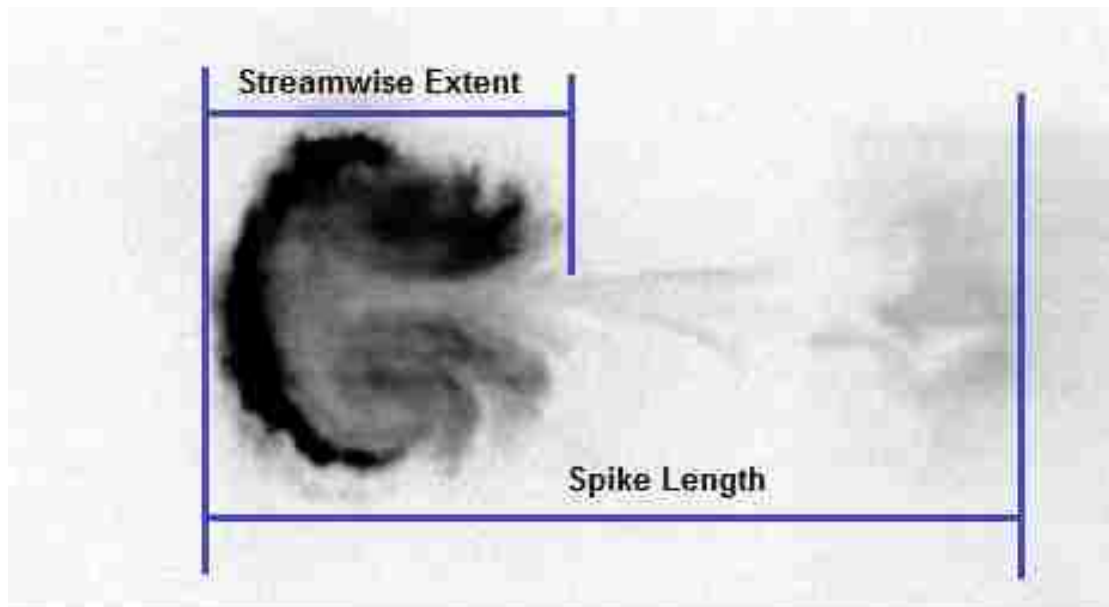


Figure 4.1.1: Measurement of the streamwise extent and spike length of an RMI image.

4.2 Angle of the Camera/Mirror

In order for the images to be collected, a mirror was mounted to the top of the test section at an angle of 45 degrees to the horizontal, as seen in Figure 4.2.1.

Previous work discussed the problem of the gas injection system preventing visualization of images in the early times. In the present work, the mirror was mounted on a rail above the test section for the mirror to slide along as the camera (and data observation points) move

downstream. The positioning of this rail also allowed for better images of the shock hitting the initial conditions, since it allowed the initial conditions to be completely viewed without obstruction.

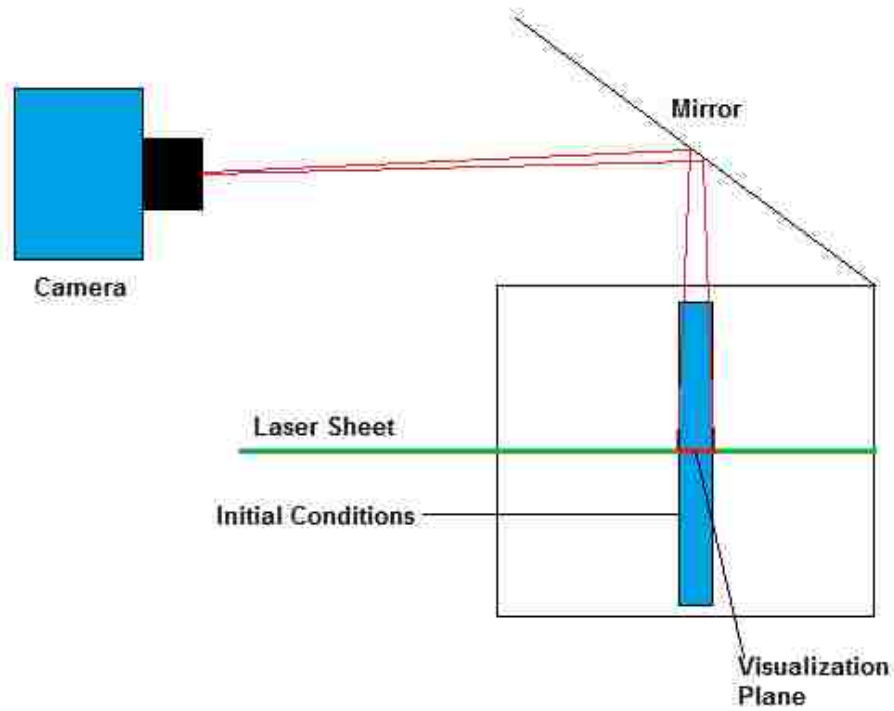


Figure 4.2.1: Layout of mirror to the top of the test section.

Chapter 5

Results

5.1 Mie Visualization

One of the key motivations for this thesis is to understand the discrepancy between the experiments using a traditional Mie tracer (like glycol droplets) and an acetone tracer compared to a numerical study mimicking the experimental conditions (as described in the previous section). Through earlier work, we have seen that the use of particles as tracers (for example, glycol fog droplets) will give serviceable results with a fair degree of accuracy [7], but with the caveat that they do not respond to the impulsive acceleration without delay and they do not show some characteristics (for example the central spike or secondary instabilities) of the RMI [8]. Indeed, Zoldi was able to show that there was a distinct difference between the area of the sulfur hexafluoride column and the actual area that the particle tracer occupied. This led to the

decision to use PLIF as the method of image collection, as the acetone tracer travelled better with the shock than the particles have done.

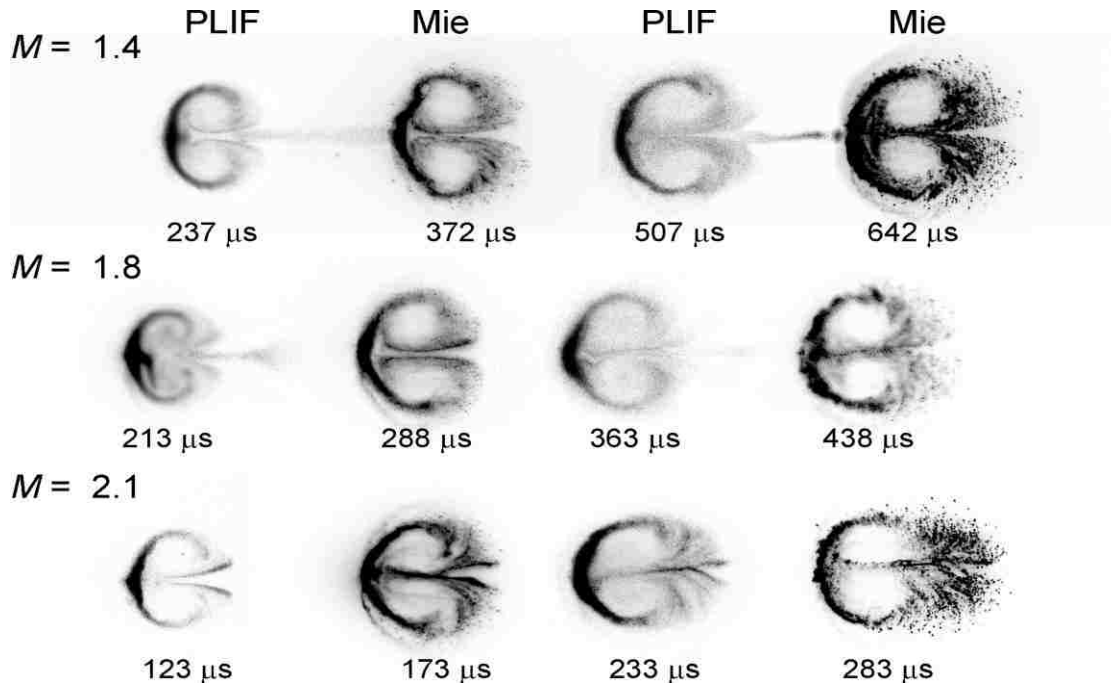


Figure 5.2.5: Experimental flow visualization using PLIF and Mie scattering of droplets for three Mach numbers. Flow direction is from left to right. Experimental images are inverted, so darker areas correspond to flow seeded with droplets (label “Mie”) or marked with acetone tracer (labeled “PLIF”). Extent of imaged area is 10.09 cm. Individual image timings (with time = 0 corresponding to shock reaching the center of the gas column) are labeled. [9]

5.2 Numerics versus Mie Scattering

Past work also highlighted the issue with particle lag, and showed that there is a delay between the shock acceleration of gases and the acceleration of the particles. This delay indicates that Mie-scattering visualization, despite being accepted as reasonably accurate at least at low Mach numbers [10] is also deficient in visualization results. To determine what Mie visualization may have omitted, a numerical model with the same experimental conditions was used to generate RMI in a perfect setting. Then the comparison between what we expect to see (numerical) and

what is actually observed (Mie experimental visualization) was conducted. It was seen that the Mie visualization omitted the central spike and small vortices at its end, as well as the secondary instabilities (KHI and baroclinic) within the counter-rotating vortex pair. These secondary instabilities enhance the conditions that lead to turbulence, so their observation and analysis, while beyond the scope of this particular thesis, is of importance to the understanding of turbulence development in fluids.

In previous work [8], modeling of the RMI was performed by using the Second-order Hydrodynamic Automatic Mesh Refinement Code (SHAMRC). SHAMRC is defined as “a two- and three-dimensional code that solves the conservation equations of fluid motion on an Eulerian grid, using operator-split explicit time-marching scheme that is second order accurate in both space and time.” [11] The equations for mass, momentum and energy conservation are divided into Lagrangian and Eulerian terms, and the solution is divided into two corresponding phases. In the Lagrangian phase, the conservation equations are solved as if we are moving with the flow for half a time step (a Lagrangian reference frame). Afterwards, any remaining energy transfer effects are applied. The results of the Lagrangian phase are then run through a Eulerian mesh, beginning the second phase. This is done like an advection calculation, where the fluxes of hydrodynamic variables are considered. As a result, the consideration of particles and/or droplets can be included in the calculation. As the experiment presented here was based on RMI-dominated flow, the consideration did not include the effects of the tracer particles in the second phase of the code.

In the model, the computational domain was limited to a two-dimensional viewpoint, representing the flow in a horizontal plane down the middle of the test section of a shock tube. The Cartesian mesh that was used for this model had a step of 0.005 cm fixed in both the

streamwise (x-) and normal-to-streamwise (y-) directions. The mesh extended from the origin (or the center of the shock tube's cross-section) to the test section walls, covering a distance of 3.81 cm in the y direction. The length of the streamwise domain used for computation was 40 cm, allowing the flow evolution to be observed for the same region as it would have been experimentally. Due to the assumption of symmetry with respect to the x-axis, only one half of the domain was modeled (the area from the x-axis centerline to the shock tube side wall). This brings the total number of required zones down to 6 million.

Air at high temperature and pressure traveling at a specific velocity were placed upstream of the initial conditions in order to generate the shock waves used in the simulations. The flow was kept steady by feeding it in from the left boundary. The gas properties that appropriate for Mach 1.7 and Mach 2.1 were generated using Rankine-Hugoniot relations.

For this experiment, the initial conditions were treated as an ideal gas with density $\rho_1 = 3.675 \text{ kg/m}^3$ and the gas constant $\gamma_1 = 1.4$. The density and the gas constant of the surrounding air were $\rho_2 = 1.225 \text{ kg/m}^3$ and $\gamma_2 = 1.4$. These would correspond to an Atwood number (A) of 0.5, which matches the experimental Atwood number.

5.3 Experimental Results

The following results were generated for two Mach numbers, Mach 1.7 and Mach 2.1, through the experimental process outlined above. The experimental data received was in the form of a multiple digital images of RMI obtained at different timings. These times ranged from 460 to 1500 microseconds after shock, for Mach number 1.7, and from 367 to 745 microseconds for

Mach 2.1. The distance from the initial conditions ranges from 2.168 to 29.0305 cm for Mach 1.7 and 2.688 to 13.543 cm for Mach 2.1.

Through post processing, using the screws of the test section as markers, the image scale could be accurately calculated. The post processing techniques also included background image subtraction, which would subtract a background image that was acquired before each shot from dynamic exposure. The subtracted image was run through a second automated program to distinguish the RMI from the background of the image. This program would convert the information contained in a grayscale pixel into one of two binary values based on a predetermined level of brightness assigned as the base value for illumination. Thus, the image was converted into a series of either black or white pixels, making the image clearer to view without the variations of grey created as a result of under-saturated sections of the RMI. The images were then aligned so that the start of the RMI fell within the same spot of the image. This made the measurement of the RMI characteristics significantly easier.

The general trend seen for a comparison of counter-rotating vortex length and spike length to the actual timing is that the length increases with timing (Figures 5.2.1 and 5.2.2). We see that the Mach 2.1 graph is shifted left of the Mach 1.7 graph for both figures, indicating a similar growth pattern for both Mach numbers, but letting us know that the Mach 2.1 graph is evolving faster than the Mach 1.7 graph. The evolution time of the counter-rotating vortex pair and central spike is strongly correlated to Mach number.

In contrast, when comparing both the spike length and the counter-rotating vortex pair, we see that there is an almost perfect collapse of the Mach 2.1 plot onto the Mach 1.7 plot. (Figures 5.2.3 and 5.2.4). This would suggest that the evolution of the counter-rotating vortex pair and

the central spike with distance is weakly correlated to Mach number. In other words, two RMIs at the same location down the shock tube should have roughly the same size growth of their features, despite them having different Mach numbers. This being said, the time for the two RMIs of different Mach numbers to arrive at that location/size will not be the same, as made evident by the figures 5.2.1 and 5.2.2, as the larger Mach number will arrive first.

A visual representation of what this means from an evolutionary standpoint is seen below: while it is seen that the RMI develops similarly for different Mach numbers, the actual timings at which each image are taken is considerably different. (Figure 5.2.5) According to the linear theory proposed by Richtmyer, the growth rate of the primary instability is

$$v^{imp} = -\Delta U A k a_0 \quad (5.3.1)$$

(a variant of equation 1.2.5) where ΔU is the piston velocity of the shock (or the difference between the mean velocity of the density interface before and after the shock); A is the Atwood number; a_0 is the pre-shock amplitude of the initial interface perturbation and k is the characteristic wave number. We see that v^{imp} is directly proportional to ΔU , as the other terms in the equation can be treated like constants. It is expected that as ΔU increases, v^{imp} increases as well.

For short-term growth rates, this result allows us to introduce a dimensionless time variable,

$$\tau = 2kA|\Delta U|t \quad (5.3.2)$$

t is the time after shock acceleration (or the actual timing). For multiple shocks at the same Atwood number with the same initial conditions, the plot of RMI amplitude as a function of τ

would give a normalization of the RMI plots for different Mach numbers. Using that same equation, it can be seen that there is a linear correlation between τ and the downstream distance

$$x = |\Delta U|t \tag{5.3.3}$$

For any given position, we have seen that two RMIs of different initial Mach number will have the same size primary characteristics at the same downstream position. This is due to the τ values of the RMIs being equal. To do so would require a constant value of τ , which is dependent on ΔU and t to having an inverse relationship; i.e. when the piston velocity increases, the time decreases, and when the piston value decreases, the time increases. Thus, we see that the space domain growth of a primary instability characteristic (spike, counter-rotating vortices) is a function of τ . The substitution of 5.3.3 into 5.3.2 allows us to rewrite equation 5.3.2 as

$$\tau = 2kAx \tag{5.3.4}$$

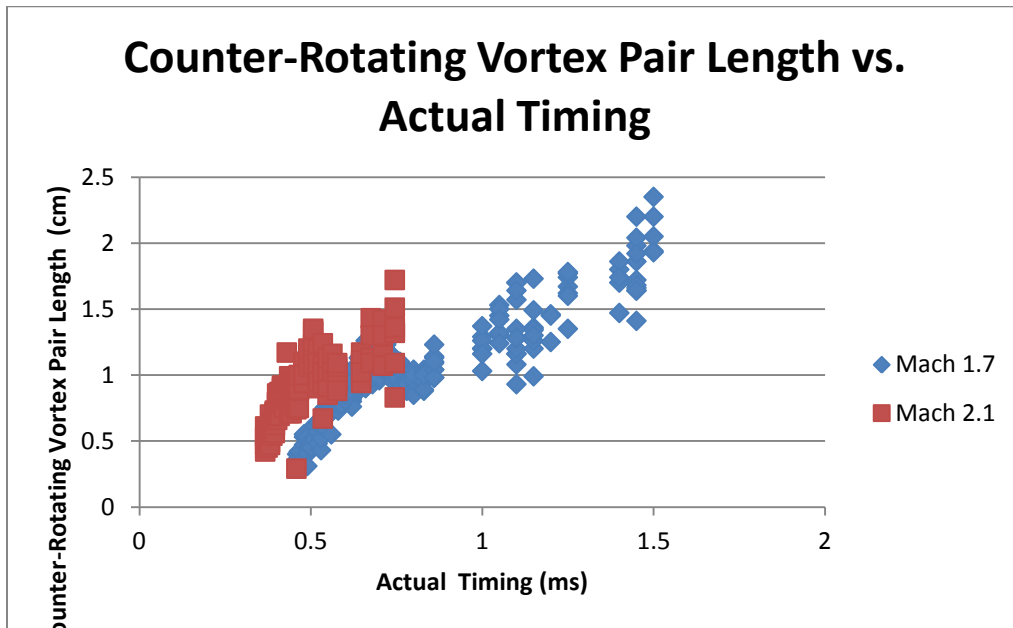


Figure 5.3.1: Plot of Counter-Rotating Vortex Pair Length vs. Actual Timing for Mach 1.7 and Mach 2.1 experimental runs.

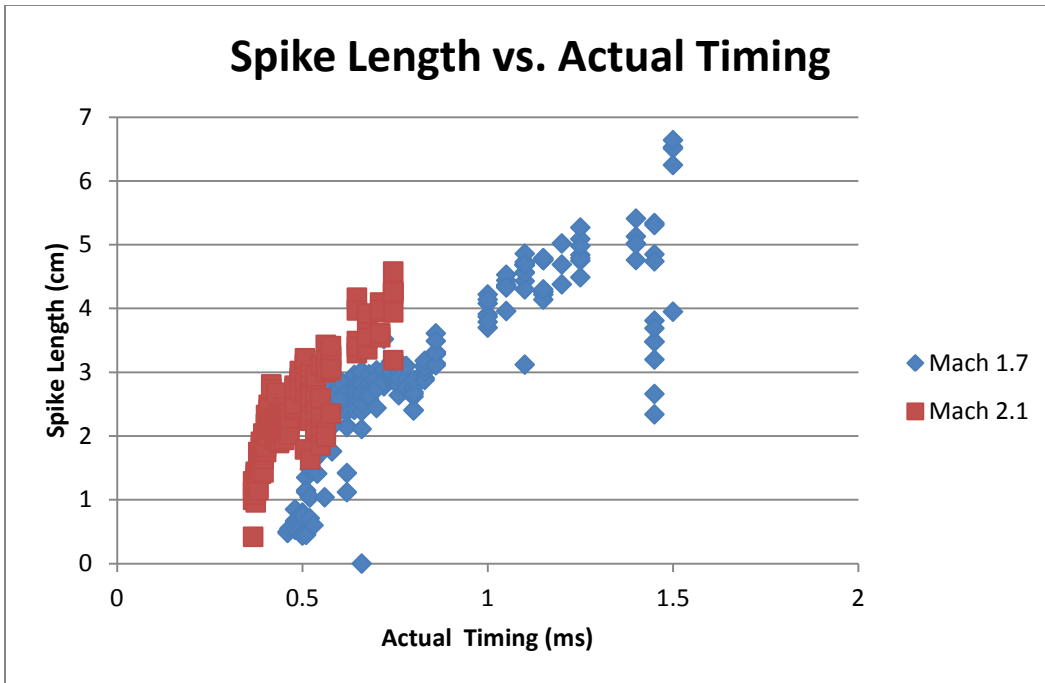


Figure 5.3.2: Plot of Spike Length vs. Actual Timing for Mach 1.7 and Mach 2.1 experimental runs.

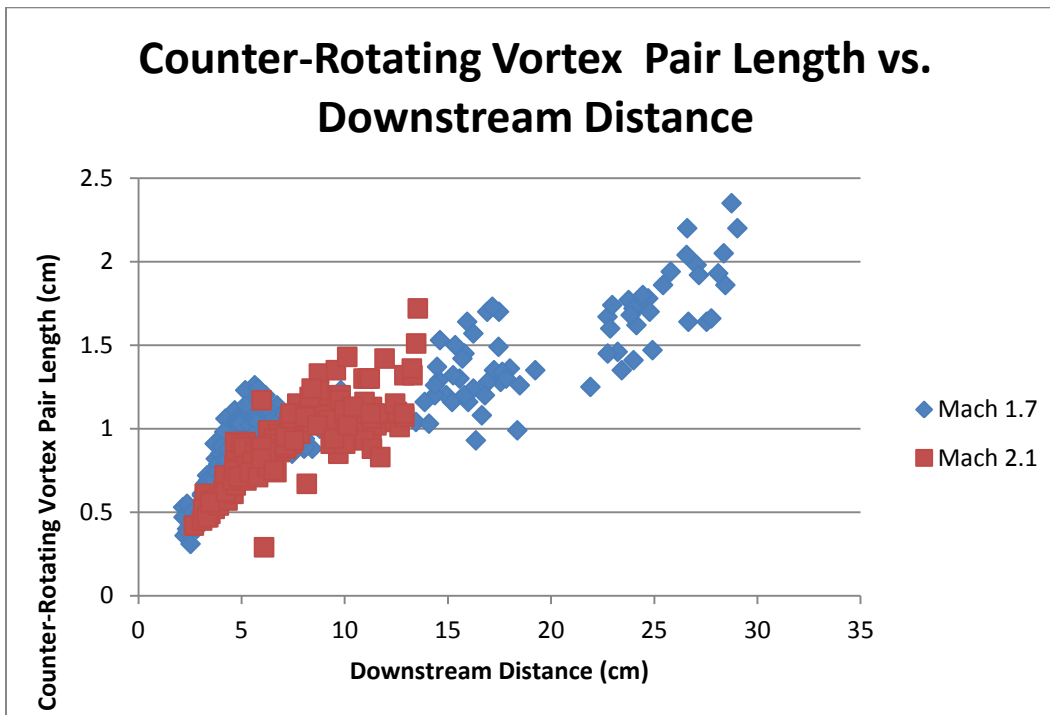


Figure 5.3.3: Plot of Counter-Rotating Vortex Pair Length vs. Downstream Distance for Mach 1.7 and Mach 2.1 experimental runs.

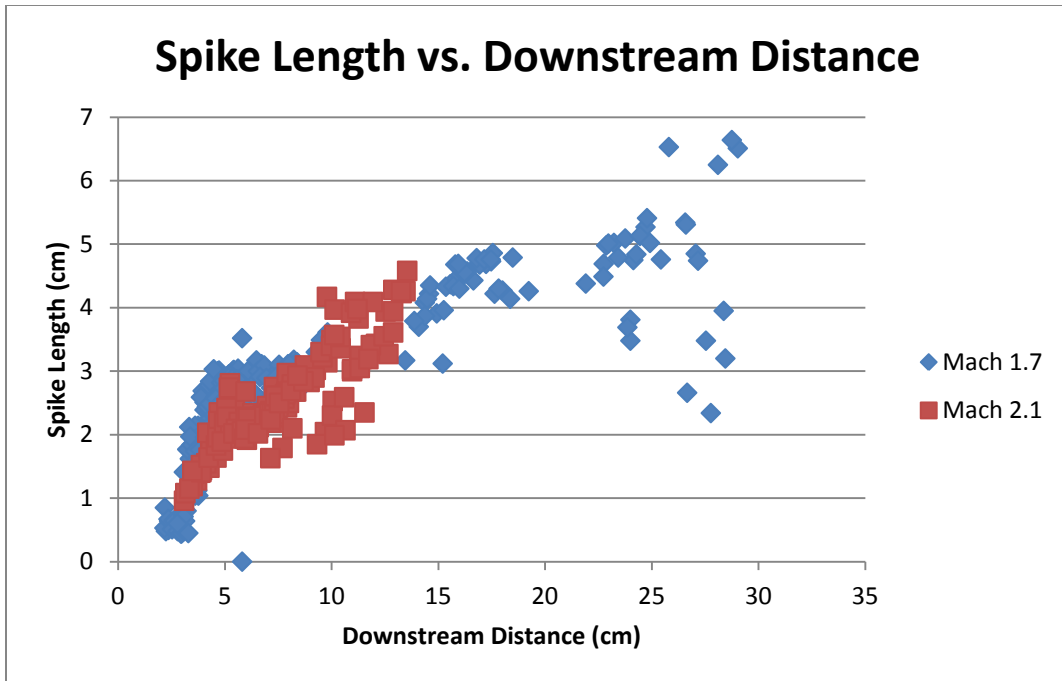


Figure 5.3.4: Plot of Spike Length vs. Downstream Distance for Mach 1.7 and Mach 2.1 experimental runs.

Chapter 6

Morphology Characteristics

6.1 RMI

In past papers, for example [12], the term “spike” was used to reference a different feature of the RMI morphology. The “spike” was a region of the perturbed interface that was occupied by the lighter gas. Abarzhi and Hermann state that in the non-linear regime, one will see a structure of bubbles and spikes appearing; bubbles appear when the light fluid penetrates the heavy fluid and a “spike” appears when the heavy fluid penetrates the light one. In their research, Abarzhi and Herrmann referred to the past research of Pavlenko (2000) [13], Chebotareva (1999) [14], Jacobs and Sheeley (1996) [15], Bonazza and Sturtevant (1996) [16]. It is very important to realize that this spike is not the same spike referred to as the “central spike” in this research. The spike discussed in this research is due to shock focusing, that is, the gaseous column of initial conditions acts as a gaseous lens, focusing the shock in the downstream direction; similar to how

a convex lens focuses light. Focusing occurs because the speed of sound in sulfur hexafluoride is much slower than that in air. More on the central spike will be discussed in Section 6.3. In review, the previous use of the term “spike” refers to the morphological behavior which occurs for all heavy into light interactions of the fluid; the central spike discussed in this thesis refers to a specific behavior that happens for heavy fluid into light fluid penetration with a gaseous initial condition column setup.

The basic morphology of RMI in a heavy gas column case is described in this section and seen visually in Figure 6.1.1. When the shock wave hits the gaseous column, initial vorticity is deposited due to the misalignment of the pressure and density gradients. The column undergoes a compression as the opposite-sign vorticity is deposited on the top and bottom edges of the compressed cylinder [11] which leads the outer ends to begin curling inwards in the direction of flow, forming the counter-rotating vortex pair.

The use of PLIF has presented better imaging of the counter-rotating vortex pair than the use of particles. Through PLIF, the observation of secondary instability development within the counter-rotating vortex pair was observed. These will be discussed later in section 6.4.

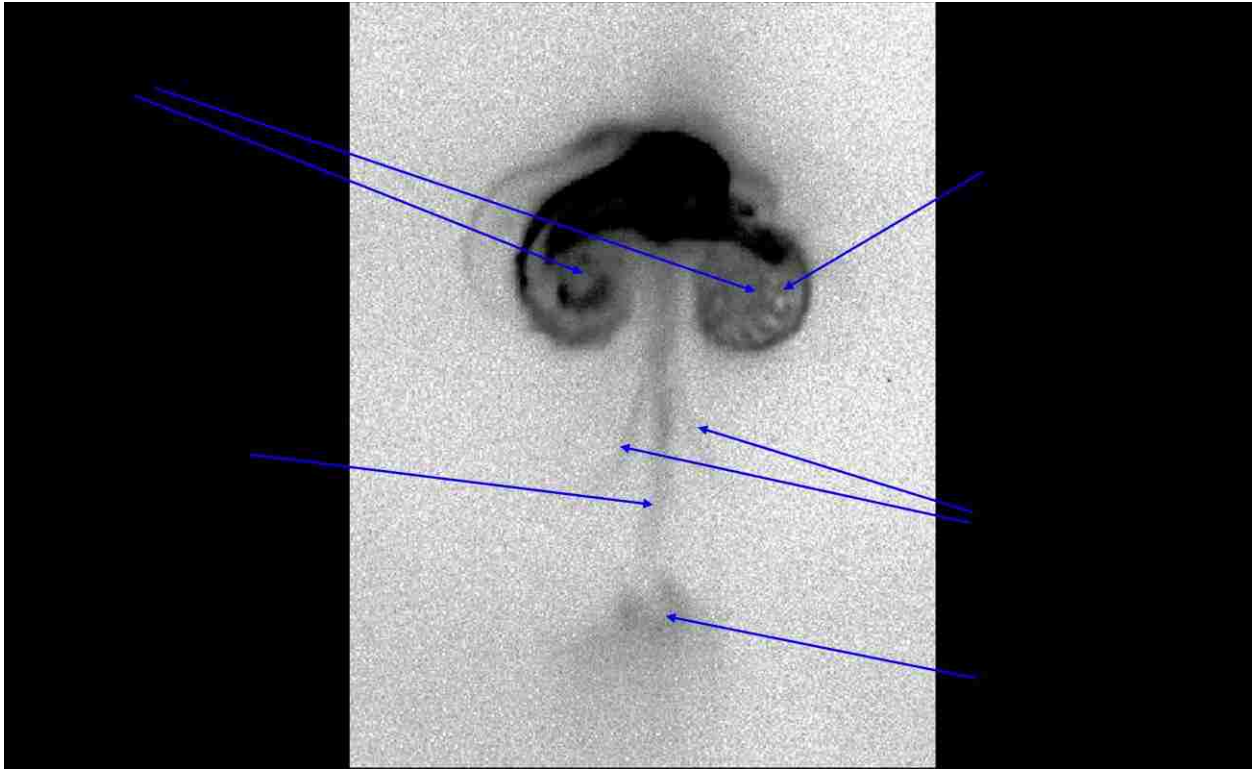


Figure 6.1.1. Inverted color image capture of an RMI with key features indicated. Note the counter-rotating vortex pair, the spike, and the lion's tail, or small scale counter-rotating vortex pair located at the end of the spike.

6.2 Growth of the Counter-Rotating Vortex Pair and Central Spike

As seen in Chapter 5, higher Mach numbers give an increase in growth of both the counter-rotating vortex pair and the central spike. By the mechanism of RMI, we know that the instability is dependent on the deposition of vorticity to develop. The increase in size of both the counter-rotating vortex pair and the central spike with higher Mach number (for the same timing) indicates that the amount of vorticity deposited also increases with increasing Mach number.

The result obtained in this experiment matches earlier results. For example, in the 2008 paper published by Balakumar, Orlicz, Tomkins and Prestridge [17], the graphical representation of structure width very much follows the shape of Figure 4.1.1. Balakumar et al. generated each point from an average of 5 measurements, while this experiment used each data point. This may explain a slight deviation from their results. Balakumar et al. observed that for a Mach 1.2 shock, there was a shock compression between $t = 15 - 30$ microseconds. This experiment's tabulated data results suggests that a compression most likely occurred as there was a decrease in central spike values at about 15 – 20 seconds after shock for Mach 1.7. In 1993, Jacobs, Jenkins, Klein and Benjamin showed the same trend in experimental results when they plotted the growth in the thickness of a sulfur hexafluoride curtain with respect to time for a Mach 1.2 shock [17]. The experimental data for the growth of the counter-rotating vortex pair agrees with previously published data as well. Prestridge, Vorobieff, Rightley and Benjamin showed that the streamwise extent with respect to time followed the same general trend as our experimental data, inasmuch as the vortex growth is concerned.

6.3 Shock Focusing

The concept of shock focusing is one that is only seen in experiments and simulations concerning a cylindrical heavy gas column subjected to “classical” RMI [17]. Shock focusing is the mechanism through which the central spike is developed [19]. Recall that the counter-rotating vortex pair contains secondary instabilities (see section 6.4) that consist of KHI and baroclinic instabilities, causing an increase in pressure buildup by the vortex pair. The cylindrical initial conditions acts the same way that a lens would, focusing the high pressure along a center-line projection downstream of the RMI. As the RMI moves to full turbulence, small scale instabilities develop on the downstream end of the spike; these then weaken due to

diffusion of the instability into the surrounding air. Figure 6.3.1 shows the conversion from initial conditions to shock focused.

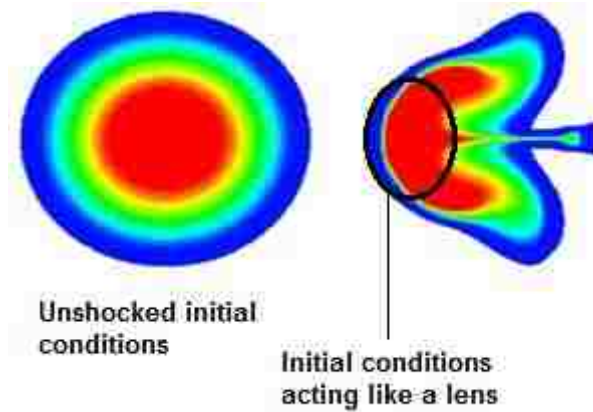


Figure 6.3.1: Numerical simulation [8] of transition from initial conditions to spike development due to shock focusing. The image on the left shows the circular pre-shock initial conditions. The image on the right includes an overlay of the initial conditions on the post-shock RMI. The initial conditions, acting as a lens, focus the high pressure region to a point of convergence down the centerline of the RMI, resulting in the formation of the shock. Convergence is usually seen for heavy gas perturbations.

6.4 Secondary Instability Development

Within the counter-rotating vortex pair, secondary instabilities were observed. These structures were not easily observed using particle tracers (due to the particle lag, and the inability of the particles to travel with the region of lower pressure and density where these secondary instabilities occur). Jacobs suggested that these instabilities were caused by a combination of shear-driven Kelvin-Helmholtz instabilities and secondary baroclinic instabilities. Each of these instabilities affect separated parts of the vortices: the KHI causes perturbations to occur at the edge of the vortex, while the baroclinic instabilities affect the vortex core. The core of the vortex is an area of low pressure, and the sulfur hexafluoride and air are transmitted by a mass

movement of horizontal air into the core, causing the pressure and density misalignment. The secondary vortex instability can ultimately develop into a three-dimensional turbulent mixing zone [20] even if the initial perturbation was two dimensional.

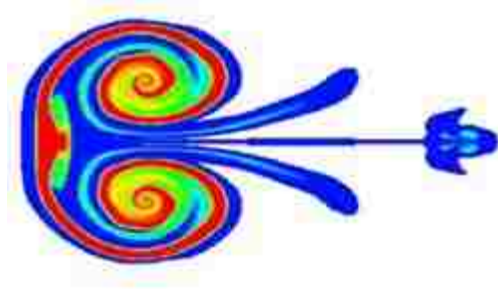


Figure 6.4.1: A numerical simulation of RMI [8]. The colored area of the counter-rotating vortex pair consists of secondary instabilities, such as KHI and baroclinic instabilities.

Chapter 7

Conclusions

In review, this thesis presented the experimental results into the investigation of fluid instabilities generated by shock acceleration into a gaseous fluid cylindrical column of sulphur hexafluoride saturated with acetone. This experiment was performed at the shock tube facility of the University of New Mexico. The images were acquired using planar laser induced fluorescence (PLIF) techniques on a horizontal plane, and the images acquired were processed by automated programs which used features of known dimensions in the images to generate a scale. Four sets of measurements were recorded for comparison between Mach numbers.

On the base level, it was seen that there was a correlation between the size of the centralized spike and the counter-rotating vortices when considering the growth of these features with respect to the actual timing of the shot. An increase in Mach number directly resulted in faster development of the same phase of the RMI than an instability of a lower Mach number: that is,

counter-rotating vortices and spikes of Mach 2.1 for the same timing were bigger than for Mach 1.7. In comparison, there was a weak correlation between the growth of these same characteristics and the downstream distance. The graphical data collapsed almost seamlessly from one Mach number to another. This suggests that, at any distance along the test section of the shock tube from the injection point, the size of the instability is the same, regardless of the Mach number. The combination of these two conclusions leads one to believe that the spatial development of RMI at any point along test section is the same despite the Mach number of the shock wave, but the timing for a shock wave to develop to that size will be different for two different Mach numbers. We can then expect a shock wave traveling at a higher initial Mach number to decompose into turbulence much quicker than a lower one, but both Mach numbers should approach turbulence at about the same location.

7.1 Future Work

As this thesis goes to print, experimental work is being performed on further discovery into the mechanism of instabilities that develop when oblique shock waves interact with a cylindrical gas column. Currently, the shock tube is tilted at an angle of 30 degrees. The intention is to collect data at multiple angles to the horizontal (from 0 degrees to 45) for comparison and to create a data repository of experimental data for multiphase fluid instabilities, specifically RMI, RTI and Kelvin-Helmholtz.

References

1. Oleg Schilling and Jeffrey W. Jacobs. (2008) "Richtmyer-Meshkov instability and re-accelerated inhomogeneous flows." *Scholarpedia*, 3(7):6090
2. Cook, Andrew W., and David Youngs. "Rayleigh-Taylor Mixing." - *Scholarpedia*. N.p., 18 Feb. 2009. Web. 10 Mar. 2014.
3. Anderson, M., Peter Vorobieff, J. Conroy, C. Truman, R. White, and S. Kumar. "An experimental and numerical study of shock interaction with a gas column seeded with droplets". *Physical Review E*. Under consideration. (2013)
4. White, Ross L. *Oblique Shock Wave Interactions With Gas Cylinder Interfaces*. Thesis. The University of New Mexico, 2012. N.p.: n.p., n.d. Print.
5. Zucker, Robert D., and Oscar Biblarz. *Fundamentals of Gas Dynamics*. Hoboken, NJ: J. Wiley, 2002. Print.
6. Richtmyer, R. D., 1960. "Taylor instability in shock acceleration of compressible fluids." *Communications in Pure and Applied Mathematics*. 13(2), pp. 297–319.
7. Rightley, P. M., P. Vorobieff, R. Martin, and R. F. Benjamin. "Experimental Observations of the Mixing Transition in a Shock-accelerated Gas Curtain." *Physics of Fluids* 11.1 (1999): 186. Web.
8. Anderson, Michael J. *Oblique Shock Interactions With Perturbed Density Interfaces*. Diss. The University of New Mexico, 2011. N.p.: n.p., n.d. Print.
9. Bernard, Tennille C., C Randall Truman, Peter Vorobieff, Clint Corbin, Patrick J. Wayne, Garrett Kuenher, Michael Anderson, and Sanjay Kumar. "Observation of the Development of Secondary Features in a Richtmyer-Meshkov Instability Driven Flow." *Journal of Fluid Engineering* (2014): n. pag. Web. (In consideration)

10. Rightley, P. M., P. Vorobieff, R. Martin, and R. F. Benjamin. "Experimental Observations of the Mixing Transition in a Shock-accelerated Gas Curtain." *Physics of Fluids* 11.1 (1999): 186. Web.
11. Vorobieff, Peter, Joseph Conroy, Michael Anderson, Ross White, Patrick Wayne, C. Randall Truman, Sanjay Kumar. "Shock-Driven Instability in Multiphase Flow." (2012)
12. Abarzhi, S. I. and M. Herrmann. "New type of the interface evolution in the Richtmyer-Meshkov instability." Center for Turbulence Research (2003)
13. Pavlenko, A. V., Baishev, A. I., Kucherenko, Y. A., Litvin, A. T. & Sorokaty, N. N. 2000. "Experimental investigation into the interaction of the stationary shock wave with the turbulent layer." *Laser Part. Beams* **18** (2), 171 -174.
14. Chebotareva, E. I., Aleshin, A. N., Zaytsev, S. G. & Sergeev, S. V. 1999. "Investigation of interaction between reflected shocks and growing perturbation on an interface". *Shock waves* **9** (2), 81-86.
15. Jacobs, J. & Sheeley, J. 1996. "Experimental study of incompressible Richtmyer-Meshkov instability." *Phys. Fluids* **8**, 405-415.
16. Bonazza, R. & Sturtevant, B. 1996. "X-ray measurements of growth rates at a gas interface accelerated by shock waves." *Phys. Fluids* **8**, 2496-2512.
17. Balakumar, B. J., G. C. Orlicz, C. D. Tomkins, and K. P. Prestridge. "Simultaneous Particle-image Velocimetry–planar Laser-induced Fluorescence Measurements of Richtmyer–Meshkov Instability Growth in a Gas Curtain with and without Reshock." *Physics of Fluids* 20.12 (2008): 124103. Print.

18. Jacobs, J. W., D. G. Jenkins, D. L. Klein, and R. F. Benjamin. "Nonlinear Growth of the Shock-accelerated Instability of a Thin Fluid Layer." *Journal of Fluid Mechanics* 295. (1995): 23 - 42. Print.
19. Chihiro Matsuoka (2014) "Kelvin-Helmholtz Instability and Roll-up." *Scholarpedia*, 9(3):11821
20. Prestridge, K., Peter Vorobieff, P. Rightley., and R. Benjamin. "Validation of an instability growth model using particle image velocimetry measurements". *Physical Review Letters* 84(19), pp. 4353–4356. (2000)
21. Brouillette, Martin. "The Richtmyer-Meshkov Instability." *Annual Rev. Fluid Mech.* 34 (2002): 445-68. Print.
22. Baltrusaitis, R. M., M. L. Gittings, R. P. Weaver, R. F. Benjamin, and J. M. Budzinski. "Simulation of Shock-generated Instabilities." *Physics of Fluids* 8.9 (1996): 2471. Print.
23. Zhai, Zhigang, Ting Si, Xisheng Luo, and Jiming Yang. "On the Evolution of Spherical Gas Interfaces Accelerated by a Planar Shock Wave." *Physics of Fluids* 23.8 (2011): 084104. Print.
24. Vorobieff, P., M. Anderson, J. Conroy, R. White, C. Truman, and S. Kumar. "Vortex deposition in shock-accelerated gas with particle/droplet seeding." *American Institute of Physics* 1426, 1651. (2012)
25. Prestridge, K., Peter Vorobieff., P. Rightley., and R. Benjamin. "Validation of an instability growth model using particle image velocimetry measurements". *Physical Review Letters* 84(19), pp. 4353–4356. (2000)

26. Vorobieff, P., M. Anderson, J. Conroy, C. Truman, R. White, and S. Kumar. "Vortex formation in a shock-accelerated gas induced by particle seeding". *Physical Review Letters* 106(18), p. 184503. (2011)
27. Tomkins, C., K. Prestridge, P. Rightley, M. Marr-Lyon, P. Vorobieff, and R. Benjamin. "A Quantitative Study of the Interaction of Two Richtmyer–Meshkov-unstable Gas Cylinders." *Physics of Fluids* 15.4 (2003): 986 - 1004. Print.
28. Rightley, P. M., P. Vorobieff, and R. F. Benjamin. "Evolution of a Shock-accelerated Thin Fluid Layer." *Physics of Fluids* 9.6 (1997): 1770 - 1782. Print.
29. Rightley, P. M., P. Vorobieff, R. Martin, and R. F. Benjamin. "Experimental Observations of the Mixing Transition in a Shock-accelerated Gas Curtain." *Physics of Fluids* 11.1 (1999): 186. Web.
30. Bernard, Tennille, Patrick Wayne, Clint Corbin, C. Randall Truman, Peter Vorobieff, Sanjay Kumar, and Michael Anderson. "Shock-accelerated Gas Cylinder: A Mach Number Study." Proc. Of American Physical Society – Division of Fluid Dynamics, Annual Meeting San Diego, CA. (2012)
31. Bar-Meir, Genick. *Fundamentals of Compressible Fluid Mechanics*. 2006. Web. 24 Mar. 2014. <<http://web.iitd.ac.in/~pmvs/mel7152008/text.pdf>>.
32. Wikipedia contributors. "John William Strutt, 3rd Baron Rayleigh." Wikipedia, The Free Encyclopedia. *Wikipedia, The Free Encyclopedia*, 16 Mar. 2014. Web. 31 Mar. 2014.
33. "Search Results." *Emilio Segrè Visual Archives*. N.p., n.d. Web. 30 Mar. 2014. <<http://photos.aip.org/quickSearch.jsp?qsearch=ich&group=1610>>.

34. Ukai, Satoshi, Kaushik Balakrishnan, and Suresh Menon. "On Richtmyer–Meshkov Instability in Dilute Gas-particle Mixtures."
35. "Lord Kelvin (1824-1907)." Lord Kelvin Biography. N.p., n.d. Web. 30 Mar. 2014. <<http://digital.nls.uk/scientists/biographies/lord-kelvin/>>. *Physics of Fluids* 22.10 (2010): 104103. Print.
36. "Hermann Von Helmholtz." Hermann Von Helmholtz. N.p., n.d. Web. 30 Mar. 2014. <<http://www.nndb.com/people/445/000072229/>>.
37. Pavlenko, A. V., Baishev, A. I., Kucherenko, Y. A., Litvin, A. T. & Sorokatyi, N. N. 2000. "Experimental investigation into the interaction of the stationary shock wave with the turbulent layer." *Laser Part. Beams* **18** (2), 171 -174.
38. Chebotareva, E. I., Aleshin, A. N., Zaytsev, S. G. & Sergeev, S. V. 1999. "Investigation of interaction between reflected shocks and growing perturbation on an interface". *Shock waves* **9** (2), 81-86.
39. Jacobs, J. & Sheeley, J. 1996. "Experimental study of incompressible Richtmyer-Meshkov instability." *Phys. Fluids* **8**, 405-415.
40. Bonazza, R. & Sturtevant, B. 1996. "X-ray measurements of growth rates at a gas interface accelerated by shock waves." *Phys. Fluids* **8**, 2496-2512.
41. Ranjan, Devesh, John Niederhaus, Bradley Motl, Mark Anderson, Jason Oakley, and Riccardo Bonazza. "Experimental Investigation of Primary and Secondary Features in High-Mach-Number Shock-Bubble Interaction." *Physical Review Letters* 98.2 (2007): n. pag. Print.